THE ASTROPHYSICAL JOURNAL, 546:L49–L52, 2001 January 1

NGC 1333—PROTOSTARS, DUST SHELLS, AND TRIGGERED STAR FORMATION

GÖRAN SANDELL[1,2] AND LEWIS B. G. KNEE[3]
Received 2000 July 18; accepted 2000 October 19; published 2000 December 22

ABSTRACT

We present large ($13' \times 18'$) and sensitive continuum maps at 850 and 450 μm of the NGC 1333 star formation region. We identify 33 submillimeter sources, some of which are extended and may contain multiple condensations. Very few of the submillimeter sources have optical or near-IR counterparts. In addition to the previously known bright class 0 sources, this survey suggests that many of the fainter sources are also likely to be very young low-mass protostars. We find several dust ridges and shells formed by outflows in the cloud, and in two cases we identify protostellar sources whose formation is likely to have been triggered by powerful outflow bow shocks. Thus, outflows have influenced the structure and evolution of the cloud over the entire area we have mapped. We derive a shallow dust clump mass spectrum, with $dN/dM \propto M^{-1.4}$ down to rather low masses, suggesting a large population of dust clumps in the brown dwarf mass range.

Subject headings: circumstellar matter — dust, extinction — ISM: jets and outflows — ISM: molecules — stars: formation

1. INTRODUCTION

NGC 1333 is a star formation region containing a large number of molecular outflows (Liseau, Sandell, & Knee 1988; Knee & Sandell 2000), Herbig-Haro (HH) objects, and regions of shock-excited H_2 emission (Hodapp & Ladd 1995; Bally, Devine, & Reipurth 1996). Near-IR surveys (Aspin, Sandell, & Russell 1994; Lada, Alves, & Lada 1996) show two embedded young clusters [ages $\sim(1–2) \times 10^6$ yr] of low- to intermediate-mass stars, one south of and one within the reflection nebula. In addition to its optical/near-IR pre–main-sequence (PMS) population, the region harbors several low-mass protostars (Sandell et al. 1991, 1994; Bachiller et al. 1998b), i.e., "class 0" objects (André, Ward-Thompson, & Barsony 1993). The submillimeter continuum is the ideal way to find protostars and other dust-enshrouded PMS objects, but the complexity of the NGC 1333 region defied attempts to obtain complete maps of the whole area until the first submillimeter array cameras came into operation. Lefloch et al. (1998a) has mapped the central area around SSV 13 at 1.25 mm using the IRAM 30 m telescope. Here we present deep images covering a much larger area, $\sim 13' \times 18'$, but these images still do not cover all of the star formation activity in NGC 1333.

2. OBSERVATIONS AND DATA REDUCTION

Observations were made with the Submillimeter Common-User Bolometer Array (SCUBA; Holland et al. 1999) at the James Clerk Maxwell Telescope[4] on 1988 February 2 and 3. The submillimeter transmission was very good but variable on the first night, but on the second night, the 450 μm transmission was poor. The observations were taken in scan-map mode: a given submap was observed by chopping in α and then in δ with throws of 20″, 30″, and 65″. Six chopped images were made in each of three submaps. Flux calibration was based on the nearby secondary calibrator CRL 618.

Each submap was reduced and calibrated individually. Submap pointing offsets were corrected by registering to the positions of the sources IRAS 4A, 4B, and 2A. Maps with the same chop throw were then added together and restored in Fourier space to form the final map. The rms noise level of the final maps are $\sim$20 mJy beam^{-1} at 850 μm and $\sim$200 mJy beam^{-1} at 450 μm. The calibration uncertainty is $\sim$15% at 850 μm and $\sim$40% at 450 μm. Our calibration agrees quite well with that of Sandell et al. (1991, 1994) and Chandler & Richer (2000), but not with (Smith et al. 2000), who find 3 times higher flux densities at 450 μm for the IRAS 4 region.

The final maps show some residual baseline uncertainties (Fig. 1), which could not be removed in the data reduction. The extended dust emission is thus unreliable, but positions and flux densities of "compact" sources are not affected. We have fitted elliptical Gaussians to all sources smaller than $\sim$30″ using the MIRIAD task IMFIT. We have also deconvolved the images using CLEAN with a symmetric model beam composed of three Gaussians, allowing us to resolve some of the blended sources. The agreement between Gaussian fits on the "raw" and the CLEANed images is very good. In Table 1, we give source positions, sizes, and background-subtracted integrated flux densities derived from Gaussian fits.

Mass estimates were derived from graybody fits to the flux densities (Sandell 2000) assuming the "Hildebrand" mass opacity (Hildebrand 1983). For most sources, we assumed a dust temperature of 25 K. For sources with clear *IRAS* counterparts, we adopted the dust temperatures derived from the *IRAS* colors (Jennings et al. 1987). Almost all sources can be fitted with optically thin dust, with the dust emissivity index β in the range of 0.8–1.5 (but not IRAS 4A; see below). A few sources appear to have low β (<0.8), suggesting that they have unusual dust properties or that they are much colder than 25 K.

3. RESULTS AND DISCUSSION

The 850 μm map (Fig. 1) gives an overview of the dust emission in NGC 1333. The strongest emission is found in the south and is associated with IRAS 2, 3 (SSV 13), and 4. Each

[1] National Radio Astronomy Observatory, P.O. Box 2, Green Bank, WV 24944.
[2] Current address: Universities Space Research Association, NASA Ames Research Center, MS 144-2, Moffett Field, CA 94035; gsandell@mail.arc.nasa.gov.
[3] National Research Council of Canada, Herzberg Institute of Astrophysics, Dominion Radio Astrophysical Observatory, 717 White Lake Road, Penticton, BC V2A 6K3, Canada; lewis.knee@hia.nrc.ca.
[4] The James Clerk Maxwell Telescope is operated on a joint basis between the UK Particle Physics and Astronomy Research Council, the Netherlands Organization for the Advancement of Pure Research, the Canadian National Research Council, and the University of Hawaii.

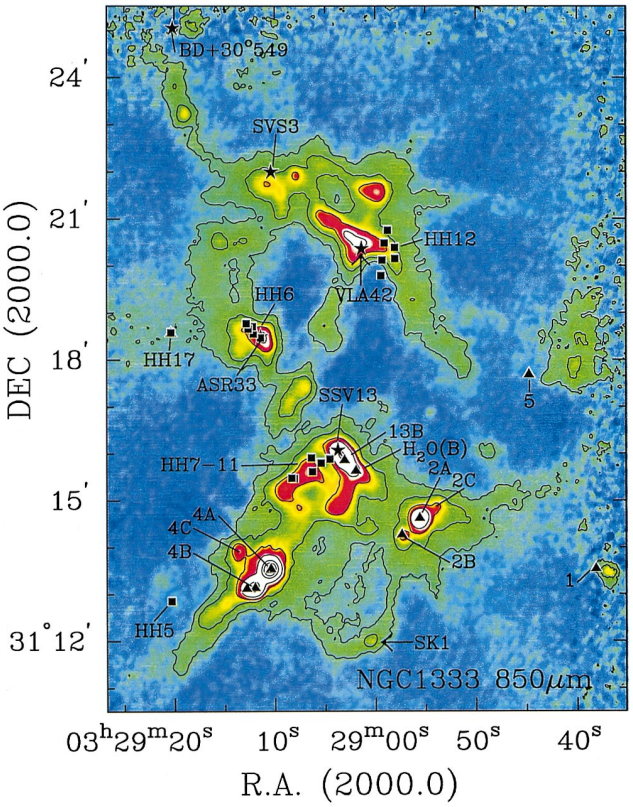

FIG. 1.—The 850 μm image of NGC 1333 in color overlaid with contours. Contour levels are 0.075, 0.225, 0.5, 1, 3, 5, and 7.5 Jy beam^{-1}. HH objects are denoted as filled squares, PMS stars as filled stars, *IRAS* sources and/or known protostars as filled triangles. The two arrows highlight proposed examples of triggered star formation: the dust ridge near the HH 12 bow shock and the object SK 1 in the southern dust shell.

of these *IRAS* sources is resolved into multiple compact sources that are surrounded by strong extended emission. A dust ridge extends from SSV 13 to IRAS 4 and beyond. A fainter ridge connects SSV 13 to IRAS 2. Other concentrations of dust are found near HH 6, HH 12, and IRAS 8 (SVS 3). Although IRAS 8 is the strongest far-IR source in NGC 1333 (Harvey, Wilking, & Joy 1984), it is not detected in the submillimeter. Our maps show a cluster of faint sources immediately south of IRAS 8. From this complex, there is a faint arc of dust emission curving to the north toward BD +30°549. Embedded in this arc are several compact sources.

The well-known shell/cavity north of SSV 13 (Ho & Barrett 1980; Langer, Castets, & Lefloch 1996; Warin et al. 1996; Lefloch et al. 1998a) is very prominent in our maps. Knee & Sandell (2000) show that this cavity is filled with high-velocity gas from several outflows (see also Warin et al. 1996). Our maps also confirm the dust shell south of SSV 13 proposed by Lefloch et al. (1998a). Several smaller cavities are also seen in the northern part of the cloud: one is seen north of IRAS 7 (ASR 33), with another to the south. The latter cavity is less pronounced because there is very little dust emission to the southeast of IRAS 7. This bipolar cavity is almost certainly caused by the large outflow from the class I object ASR 33 (Knee & Sandell 2000), 21 in Table 1. Another small cavity lies between SVS 3 and IRAS 6 (VLA 42) and is bounded by a ring of faint sources (26, 27, 29, 30, and 31).

3.1. *The Main Protostellar Concentrations*

The IRAS 2 region.—We resolve IRAS 2 into three sources: IRAS 2A (8) and 2B (7) are previously known (Sandell et al. 1994; Blake et al. 1995; Lefloch et al. 1998a; Rodríguez, Anglada, & Curiel 1999), and 2C (9) is detected here for the first time. IRAS 2A is a class 0 object driving a bipolar molecular jet (Sandell et al. 1994; Ward-Thompson et al. 1996; Bachiller et al. 1998a); the bow shock of the eastern jet is detected in our SCUBA maps. Rodríguez et al. (1999) suggest that the centimeter-wave emission from IRAS 2A may be dominated by thermal dust emission. However, its 850 μm emission, when interpreted in terms of optically thin dust with $\beta \sim 1.5$, predicts a dust continuum flux density of $\sim$1 μJy at 6 cm, far less than what is observed. The fainter IRAS 2B is likely to drive a jetlike bipolar molecular outflow (Knee & Sandell 2000) and is thus a possible class 0 source. Knee & Sandell (2000) identify IRAS 2C as the driving source of the large IRAS 2 NNE-SSW CO outflow.

The SSV 13 region.—In agreement with Chini et al. (1997), our 450 μm map resolves the SSV 13 ridge into three sources (Fig. 2). However, unlike their 1.25 mm results, we find that the class 0 object SSV 13B (12) is brighter than SSV 13 (13) at 850 μm. SSV 13B is cold and has a low β, in good agreement with the IRAM interferometer results at 3.5 and 1.3 mm (Bachiller et al. 1998b). H_2O(B), the third submillimeter source in the ridge, is not detected in the near-IR, which suggests that it is also a class 0 object. Knee & Sandell (2000) propose that an outflow from H_2O(B) is involved in the creation of the large dust shell south of the ridge. The dust emission near H_2O(B) traces a shell-like structure opening up from the star toward the south (Fig. 2), consistent with this scenario.

The IRAS 4 region.—Our SCUBA maps of the IRAS 4 region look very similar to the UKT 14 maps presented by Sandell et al. (1991) and the 1.3 mm map of Lefloch et al. (1998a). At 450 μm, IRAS 4A (4) is only slightly extended considering that it is a binary system (Lay, Carlstrom, & Hills 1995; Looney, Mundy, & Welch 2000). Its dust emission is significantly optically thick even at 850 μm ($\tau_{850} \sim 0.2$–0.5) and $\beta \sim 1.3$, for $T \sim 20$–30 K. This extreme protostellar binary cannot be well modeled with an isothermal model. We derive a mass of $\sim$1.5 $M_\odot$, less than that of Sandell et al. (1991) because we assume a smaller distance of 220 pc to NGC 1333 (Černis 1990) and do a better subtraction of the underlying cloud. Most of the centimeter-wave emission from IRAS 4A may be thermal dust emission rather than free-free emission (Mundy et al. 1993). We resolve IRAS 4B into a double system separated by $\sim$10″. The western component (4BW; 3 in Table 1) is a class 0 object driving a compact bipolar outflow and is associated with free-free emission (Mundy et al. 1993; Blake et al. 1995; Rodríguez et al. 1999). The eastern component (4BE; 2 in Table 1) is not detected in the centimeter wave nor does it drive a known outflow. The low-mass compact object IRAS 4C is more extended than 4A or 4BW, which is perhaps why it has not yet been detected in sensitive 3 mm aperture synthesis maps (Looney et al. 2000). This and the presence of free-free emission and the signature of infall (Mardones 1998) suggest that it is a class 0 object.

3.2. *The Key Role of Outflows in NGC 1333*

Large-scale imaging of regions forming high-mass stars (Johnstone & Bally 1999; Sandell 2000) or low-mass stars (Casali, Eiroa, & Duncan 1993; White, Casali, & Eiroa 1995;

TABLE 1

POSITIONS AND INTEGRATED FLUX DENSITIES OF COMPACT SOURCES IN THE NGC 1333 FIELD

Number	α(2000.0)	δ(2000.0)	$\theta_a \times \theta_b$ (arcsec)	P.A. (deg)	S_{850} (Jy)	S_{450} (Jy)	β	M_{tot} ($M_\odot$)	Other Name or Associated Object
1	03 29 00.51	+31 12 00.6	11.2 × 4.1	−46	0.34	2.23	1.09	0.07	
2	03 29 12.88	+31 13 08.2	8.6 × 2.6	+15	1.02	5.52	1.14	0.14	IRAS 4BE
3	03 29 12.02	+31 13 08.7	6.8 × 2.9	−26	3.62	17.2	1.11	0.49	IRAS 4BW, VLA 28
4[a]	03 29 10.50	+31 13 31.7	7.1 × 2.7	−34	9.05	29.7	1.28	1.5	IRAS 4A, VLA 25
5	03 29 13.64	+31 13 57.5	8.6 × 6.0	+80	0.93	3.95	1.43	0.15	IRAS 4C, VLA 29
6[b]	03 28 37.00	+31 13 27.5	Point source?	…	0.43	2.2	1.09	0.06	IRAS 1?
7	03 28 57.31	+31 14 14.3	7.6 × 5.0	0	0.45	1.75	0.63	0.03	IRAS 2B, VLA 10
8	03 28 55.61	+31 14 36.9	9.8 × 5.5	−15	3.27	23.7	1.37	0.35	IRAS 2A, VLA 7
9[c]	03 28 53.90	+31 14 53.5	11.1 × 7.6	−67	0.37	2.38	1.27	0.05	IRAS 2C
10	03 29 00.80	+31 14 24.4	Point source	…	0.10	…	…	…	IRAS 2 eastern bow shock
11	03 29 01.97	+31 15 37.4	8.5 × 6.9	…	0.50	4.06	1.62	0.10	H_2O(B), MMS 3, VLA 2
12	03 29 03.05	+31 15 52.5	10.4 × 8.3	+15	3.52	14.3	0.85	0.23	SSV 13B, MMS 2, VLA 17
13	03 29 03.73	+31 16 03.0	5.9 × 5.2	−71	2.52	14.8	0.80	0.13	SSV 13, MMS 1, VLA 4
14	03 29 04.18	+31 14 51.0	Point source	…	0.22	0.55	0.73	0.01	
15	03 29 06.31	+31 15 38.2	18 × 10	+29	0.82	4.46	1.12	0.11	HH 8
16	03 29 08.90	+31 15 20.8	26 × 14	−30	1.81	8.84	0.95	0.20	Near HH 7
17	03 29 08.78	+31 17 59.5	25 × 25	…	1.97	9.28	1.27	0.63	Peak in COR 1
18	03 29 07.06	+31 17 25.6	20 × 15	−14	0.98	4.67	1.29	0.32	Peak in COR 1
19[b]	03 28 40.29	+31 17 52.3	14 × 8	−16	0.29	3.70	2.10	0.05	IRAS 5
20	03 29 10.82	+31 18 19.5	7.0 × 6.5	+45	0.58	3.58	1.32	0.10	IRAS 7 SM 2
21	03 29 11.31	+31 18 31.1	8.0 × 5.6	−49	0.93	5.45	0.99	0.06	IRAS 7 SM 1, ASR 33, VLA 27
22[d]	03 29 15.64	+31 20 30.8	26 × 15	0	0.67	2.81	0.72	0.06	
23	03 29 02.04	+31 20 09.6	11 × 11	+16	1.01	7.23	1.54	0.23	IRAS 6
24	03 29 01.26	+31 20 28.9	25 × 14	+88	2.41	19.0	1.49	0.31	IRAS 6, VLA 42
25	03 29 02.78	+31 20 40.0	15 × 7.0	+63	1.21	4.56	1.99	0.19	IRAS 6
26[e]	03 29 04.75	+31 20 59.0	60 × 22	+62	5.42	38.0	1.50	1.18	
27[f]	03 29 09.52	+31 21 27.7	18.6 × 12.1	−21	0.47	2.33	0.98	0.05	
28[g]	03 29 10.78	+31 21 43.8	30 × 18	−88	1.19	9.09	1.63	0.30	
29	03 29 07.93	+31 21 55.5	8.0 × 5.5	+11	0.32	1.21	0.73	0.04	
30[h]	03 29 05.64	+31 22 15.5	13 × 9	…	0.19	1.12	1.24	0.03	
31[i]	03 28 59.63	+31 21 33.9	16 × 13	…	1.58	6.87	0.94	0.24	
32	03 29 19.04	+31 23 13.7	11 × 10	…	0.58	3.13	1.10	0.08	
33[b]	03 29 18.28	+31 25 06.3	23 × 20	…	0.95	…	…	…	

NOTE.—Units of right ascension are hours, minutes, and seconds, and units of declination are degrees, arcminutes, and arcseconds.

[a] Binary with separation 1″.8 (see Lay et al. 1995).

[b] Near edge of field (unreliable flux densities).

[c] Position from 850 μm (size and flux uncertain).

[d] Difference in morphology between 850 and 450 μm ("jetlike" extension to the west).

[e] Extended core (likely to contain several embedded "sources").

[f] Blend with 28 (size and flux density uncertain). Part of "streamer" extending to the south.

[g] Difference in morphology between 850 and 450 μm (multiple?), blend with 27.

[h] Source size uncertain (faint source embedded in extended filament).

[i] Source in elongated cloud core with jetlike extension to the east (possibly a second source).

Motte, André, & Neri 1998; Wilson et al. 1999) shows, in both cases, a very lumpy and filamentary cloud structure, in agreement with recent models of the initial collapse and fragmentation of a molecular cloud (Klessen, Burkert, & Bate 1998) leading to the clustered mode of star formation. Furthermore, these model calculations show a good agreement with the observationally determined mass spectrum ($\alpha \sim 1.5$). Such lumpy filaments are present in our SCUBA maps of NGC 1333, but in addition we see shells/cavities that have been created by outflows. Clearly, the large-scale structure of NGC 1333 has been considerably modified and disrupted by multiple outflows, and, apart from presumably increasing the levels of cloud-supporting turbulence, we suggest that these compressed dust shells result in the formation of new generations of stars that disrupt the cloud even further. Our results thus support the hypothesis that NGC 1333 is an example of self-regulated star formation (Norman & Silk 1980; Silk 1995).

We can suggest specific examples of star formation events triggered by outflow-driven shells in NGC 1333. Source 1 (labeled "SK 1" in Fig. 1) is embedded in the dust shell south of the SSV 13 ridge and appears to be a case of triggered star formation. The measured mass of SK 1, $\sim$0.07 $M_\odot$, is much less than its virial mass, $\sim$0.2–1 $M_\odot$ (with an assumed line width of 0.5–1 km s^{-1} (Warin et al. 1996; Lefloch et al. 1998b). We suggest that the collapse of this otherwise gravitationally stable clump has been caused by the pressure from the stellar wind(s) that have presumably created the dust shell. A second example may be in the region of the bow shock near HH 12. The centimeter-wave source VLA 42 (Rodríguez et al. 1999) lies within 2″.5 of the very strong 450 μm submillimeter source 24. Its apparent youth and location near the tip of the HH 12 bow shock suggests that its collapse may also have been triggered. Further observations of these newly discovered triggered star formation candidates are urged.

3.3. *The Mass Spectrum*

Recent millimeter-wave continuum mapping of dust cores in the ρ Oph (Motte et al. 1998) and Serpens (Testi & Sargent 1998) star formation regions suggest that their mass spectrum $dN/dM \propto M^{-\alpha}$ matches rather well the stellar initial mass function (IMF): for masses $\gtrsim$0.5 $M_\odot$, both ρ Oph and Serpens have

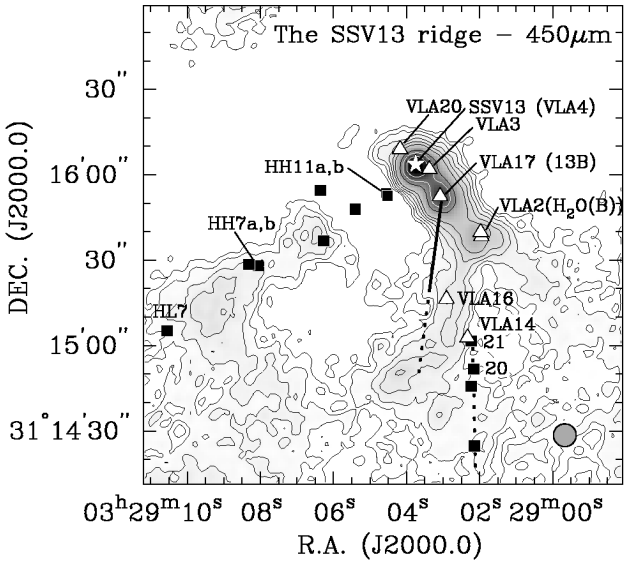

FIG. 2.—CLEANed 450 μm map of the SSV 13 area, restored with an 8″ symmetric Gaussian beam, resolving the SSV 13 ridge into three sources at 450 μm. The peak flux in this map is 11 Jy beam^{-1}. Contour levels are 0.6, 0.8, 1.06, 1.42, 1.90, 2.53, and 4.50 Jy beam^{-1}. HH objects are denoted as filled squares, and VLA sources as open triangles. The H_2 jet south of SSV 13 C (*dotted line*) is outlined by the near-IR nebulosities ASR 20 and 21 (Aspin et al. 1994) and by additional knots from Hodapp & Ladd (1995). The direction and extent of the SiO jet from SSV 13B (Bachiller et al. 1998b) are represented by a solid line with a dotted extrapolation.

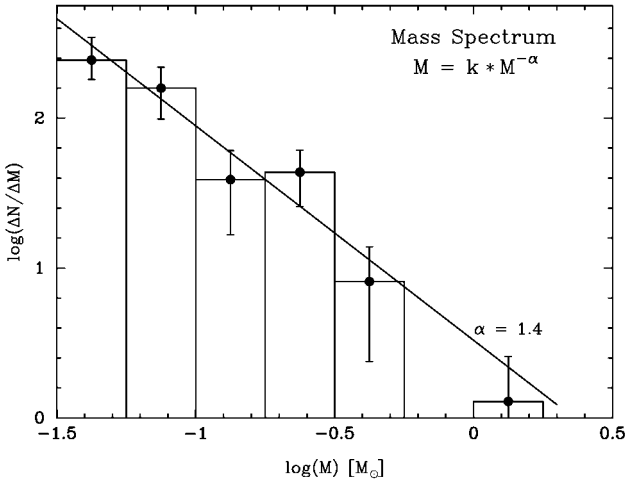

FIG. 3.—Mass spectrum of compact sources in NGC 1333 with the power-law fit superposed. The error bars correspond to $\sqrt{N}$ counting statistics.

$\alpha \sim 2.5$. The Serpens survey was limited in sensitivity to clumps $\gtrsim 0.5\ M_\odot$ and thus could not determine whether, like the stellar IMF, the clump mass spectrum flattens at lower masses. The ρ Oph survey is complete down to $\sim 0.1\ M_\odot$ and indicates that α does flatten to ~1.5. An important question is what happens to the mass spectrum below $\sim 0.1\ M_\odot$, i.e., for clumps that have the masses of brown dwarfs (objects below the stellar hydrogen-burning limit). Our survey of NGC 1333 is complete down to nearly $0.01\ M_\odot$ and has $\alpha = 1.4 \pm 0.2$ from that limit up to $\sim 0.5\ M_\odot$ (Fig. 3). Although we must be cautious when considering the relatively small number of objects in our sample, we see no evidence for a precipitous decline in clump mass spectrum below the hydrogen-burning limit, in agreement with the ρ Oph stellar IMF (Luhman & Rieke 1999). It appears that the NGC 1333 region contains a very substantial population of dust clumps in the brown dwarf mass range.

The National Radio Astronomy Observatory is a facility of the National Science Foundation operated under cooperative agreement by Associated Universities, Inc.

REFERENCES

André, P., Ward-Thompson, D., & Barsony, M. 1993, ApJ, 406, 122
Aspin, C., Sandell, G., & Russell, A. P. G. 1994, A&AS, 106, 165
Bachiller, R., Codella, C., Colomer, F., Liechti, S., & Walmsley, C. M. 1998a, A&A, 335, 266
Bachiller, R., Guilloteau, S., Gueth, F., Tafalla, M., Dutrey, A., Codella, C., & Castets, A. 1998b, A&A, 339, L49
Bally, J., Devine, D., & Reipurth, B. 1996, ApJ, 473, L49
Blake, G. A., Sandell, G., van Dishoeck, E. F., Groesbeck, T. D., Mundy, L., & Aspin, C. 1995, ApJ, 441, 689
Casali, M. M., Eiroa, C., & Duncan, W. D. 1993, A&A, 275, 195
Černis, K. 1990, Ap&SS, 166, 315
Chandler, C., & Richer, J. S. 2000, ApJ, 530, 851
Chini, R., Reipurth, B., Sievers, A., Ward-Thompson, D., Haslam, C. G. T., Kreysa, E., & Lemke, R. 1997, A&A, 325, 542
Harvey, P. M., Wilking, B. A., & Joy, M. 1984, ApJ, 278, 156
Hildebrand, R. H. 1983, QJRAS, 24, 267
Ho, P. T. P., & Barrett, A. H. 1980, ApJ, 237, 38
Hodapp, K. W., & Ladd, E. F. 1995, ApJ, 453, 715
Holland, W. S., et al. 1999, MNRAS, 303, 659
Jennings, R. E., Cameron, D. M., Cudlip, W., & Hirst, C. J. 1987, MNRAS, 226, 461
Johnstone, D., & Bally, J. 1999, ApJ, 510, L49
Klessen, R. S., Burkert, A., & Bate, M. R. 1998, ApJ, 501, L205
Knee, L. B. G., & Sandell, G. 2000, A&A, in press
Lada, C. J., Alves, A., & Lada, E. A. 1996, AJ, 111, 1964
Langer, W. D., Castets, A., & Lefloch, B. 1996, ApJ, 471, L111
Lay, O. P., Carlstrom, J. E., & Hills, R. E. 1995, ApJ, 452, L73
Lefloch, B., Castets, A., Cernicharo, J., Langer, W. D., & Zylka, R. 1998a, A&A, 334, 269
Lefloch, B., Castets, A., Cernicharo, J., & Loinard, L. 1998b, ApJ, 504, L109
Liseau, R., Sandell, G., & Knee, L. B. G. 1988, A&A, 192, 153
Looney, L. W., Mundy, L. G., & Welch, W. J. 2000, ApJ, 529, 477
Luhman, K. L., & Rieke, G. H. 1999, ApJ, 525, 440
Mardones, D. 1998, Ph.D. thesis, Harvard Univ.
Motte, F., André, P., & Neri, R. 1998, A&A, 336, 150
Mundy, L. G., McMullin, J. P., Grossman, A. W., & Sandell, G. 1993, Icarus, 106, 11
Norman, C., & Silk, J. 1980, ApJ, 238, 158
Rodríguez, L. F., Anglada, G., & Curiel, S. 1999, ApJS, 125, 427
Sandell, G. 2000, A&A, 358, 242
Sandell, G., Aspin, C., Duncan, W. D., Russell, A. P. G., & Robson, E. I. 1991, ApJ, 376, L17
Sandell, G., Knee, L. B. G., Aspin, C., Robson, I. E., & Russell, A. P. G. 1994, A&A, 285, L1
Silk, J. 1995, ApJ, 438, L41
Smith, K. W., Bonnell, I. A., Emerson, J. P., & Jenness, T. 2000, MNRAS, in press
Testi, L., & Sargent, A. I. 1998, ApJ, 508, L91
Ward-Thompson, D., Buckley, H. D., Greaves, J. S., Holland, W. S., & André, P. 1996, MNRAS, 281, L53
Warin, S., Castets, A., Langer, W. D., Wilson, R. W., & Pagani, L. 1996, A&A, 306, 935
White, G. J., Casali, M. M., & Eiroa, C. 1995, A&A, 298, 594
Wilson, C. D., et al. 1999, ApJ, 513, L139